ORIGINAL ARTICLE

ASTER mapping of limestone formations and study of caves, springs and depressions in parts of Sultanate of Oman

Sankaran Rajendran · Sobhi Nasir

Abstract Caves, springs, and large depressions of limestone karst formations are becoming more attractive tourist places and have potential importance on socio-economic development. The present study is a multi-scale point of view on limestone karst, from the space images to microscopic fabric. Here, the karst features consist of limestone formations of Cretaceous (Albian–Cenomanian) age of Tanuf Valley and Tertiary (Late Paleocene–Middle Eocene) age of Sur region of parts of Sultanate of Oman which are mapped in the visible near-infrared and short-wave infrared spectral bands of advanced spaceborne thermal emission and reflection radiometer (ASTER) using decorrelated stretch image processing technique and the occurrences of caves, springs, and depressions of the formations in the field were studied. The decorrelated RGB images of ASTER spectral bands 8, 3, and 1 discriminated well the limestone formations and associated lithology. The limestone formations of Tanuf valley (Natih formations of Hajar unit) are thick-bedded, massive, shallow marine limestone and clayey limestone, which have caves and springs. Large depressions are studied as collapsed structures at the boundary between Abat formations; they consist of gray to white marly or micritic limestone with chert nodules and Seeb Formation of bioclastic limestone, calcarenite, marl, and sandstone of Sur region. Interpretations of limestone formations, their occurrences and distributions of caves, springs and depressions of these regions are verified and confirmed in the field and studied in the laboratory. Occurrences of more springs and depressions in the limestone formations of the study sites are interpreted and located on the Google Earth image. The study proved the capability of ASTER sensor in mapping of limestone formations and recommends the technique to other geographical regions where similar geological questions need to be resolved.

Introduction

Nowadays, the caves, springs and the places of large depressions that occur in carbonate massifs attract more tourists and emerging tourist places like Oman (Hanna and Al-Belushi 1996; http://www.alhotacaves.com). Springs that occur in limestone karst formations play a vital role in socio-economic cultural development of arid and semi-arid regions. Caves of carbonate formations are developed due to the dissolution of water soluble rock which occurred below the massif surfaces. Large karst depressions are the geomorphic features formed by the movement of rocks or sediments into voids created by the dissolution of water soluble rock (Waltham et al. 2005; Sauro 2003; Williams 2003; Beck 1984). Occurrence of such collapsed structures depends on the non-cohesive (sand-rich, creating slow subsidence), or cohesive (clay-rich, creating rapid subsidence) characters of overlying sediments (Sinclair and Stewart 1985). These karst features occur predominantly in limestone formations of Tanuf Valley and near Sur regions of parts of Sultanate of Oman (Fig. 1) and have considerable attention to study either for social interest or their potential socio-economic cultural importance.

Remote sensing technique is proved to map limestone formations and identify carbonate minerals (Rajendran

S. Rajendran (✉) · S. Nasir
Department of Earth Sciences, Sultan Qaboos University,
Al-Khod 123, Muscat, Oman
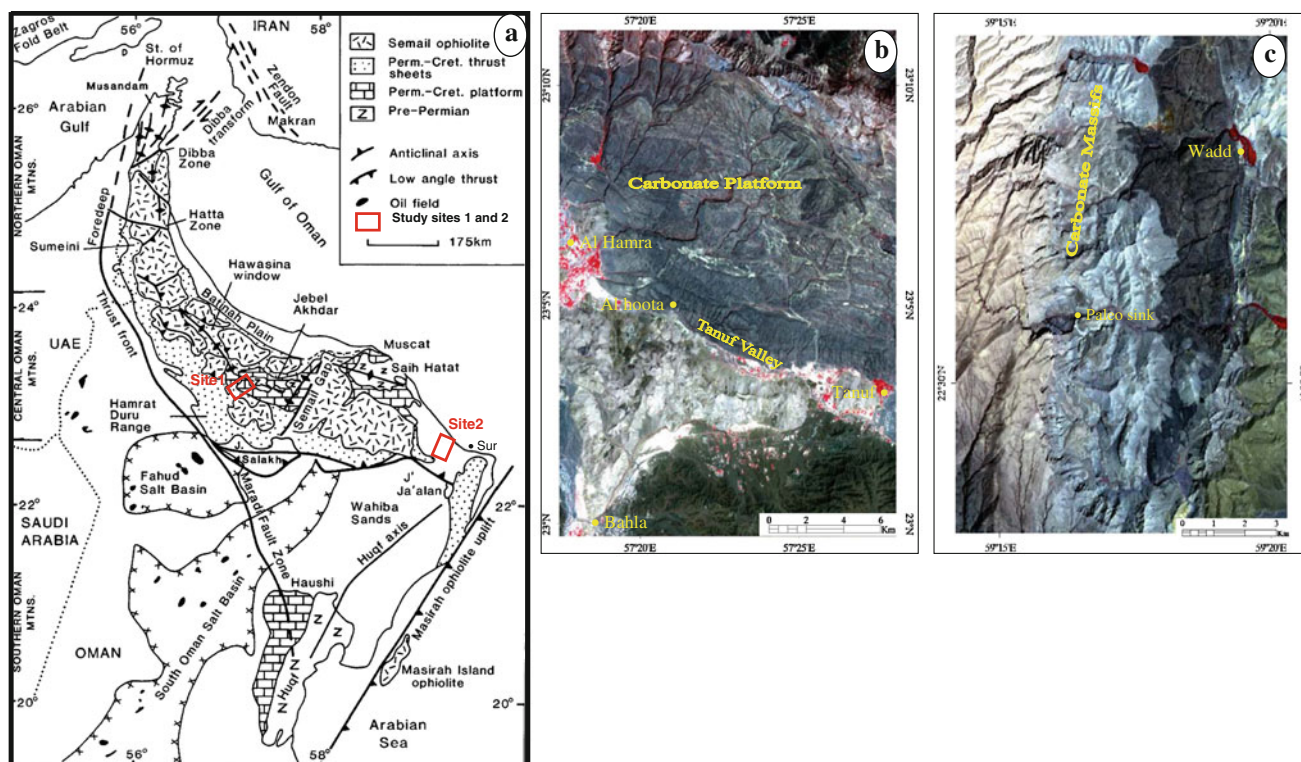e-mail: sankaranrajendran@yahoo.com

Fig. 1 Shows a regional geology and structural map of the Oman Mountain area (after Robertson and Searle 1990), b and c the ASTER FCC image (RGB bands 3, 2, and 1) illustrates the carbonate massifs of Tanuf Valley (Site. 1) and the region near to Sur (Site. 2), respectively

et al. 2011; Corrie et al. 2010; Siart et al. 2009; Jalali et al. 2009; Ninomiya et al. 2005; Gomez et al. 2005; Rowan and Mars 2003; Abdeen et al. 2001; Sultan et al. 1987). The reflectance electromagnetic spectrum in the 0.3–2.5 μm wavelengths provide mineralogical information, especially carbonate minerals that have diagnostic CO_3 spectral absorptions near 2.35 μm in the spectrum and can be used significantly to map carbonate minerals bearing rocks (Mars and Rowan 2010; Ninomiya 2002; Clark 1999; Hunt 1977). The ASTER on board the earth observing system (EOS) TERRA platform offers relatively improved spatial, spectral, and temporal resolutions and has the spectral bands 8 and 14 characteristics to the diagnostic CO_3 absorption facilitates to map carbonate rich formations (Rajendran et al. 2011). Understanding its capability, in the present study, the mapping of limestone formations of Cretaceous (Albian–Cenomanian) age of Tanuf Valley (Fig. 1a, b; Site 1) and Tertiary (Late Paleocene–Middle Eocene) age of Sur region (Fig. 1a, c; Site 2) of parts of Oman are carried out using the visible near-infrared–shortwave infrared (VNIR–SWIR) spectral bands of ASTER by decorrelated stretch digital image processing technique. The interpreted images are verified in the field for the occurrences of limestone formations. The occurrence and distribution of caves, springs, and depressions of the limestone formations of these regions are studied. Review of literature shows that a

meager study has been attempted on the application of remote sensing technique in mapping of limestone formations which are associated with these features and no study has been carried out for the said study regions.

Spectral characteristics of carbonate minerals

Carbonate minerals have favorable spectral absorption characteristics for remote identification. The reflectance spectrum of limestone formation depends on the carbonate minerals composition of its surface, which is usually a mixture of the whole formation mineralogy and weathering or alteration of minerals. Comprehensive spectral absorption-compositional studies can provide important insights to the causes of spectral variations and quantitative data for use in the interpretation of optical remote sensing data (Rajendran et al. 2011; Mars and Rowan, 2010; Corrie et al. 2010; Ninomiya et al. 2005; Rowan and Mars 2003). The spectral library plots of major carbonate minerals stacked from the USGS Spectral Library for minerals (Envi 4.8) are given in Fig. 2. The carbonate minerals such as calcite ($CaCO_3$), dolomite [CaMg $(CO_3)_2$], and siderite ($FeCO_3$) show significant useful narrow absorption features around 2.35 μm [shown by the vertical line in Fig. 2; correspondence to band 8 (2.295–2.365 μm) in ASTER

data] due to C–O bonds (Mars and Rowan 2010) in their compositions. The calcite and dolomite (end members of series) minerals can be distinguished and identified by variations in their absorptions between 2.33 and 2.45 μm (Kuosmanen et al. 2000; Mars and Rowan 2010; Combe et al. 2006). The iron carbonate, siderite shows absorption near 2.3 μm due to C–O bonds and broad absorption around 1.1 μm due to the presence of ferrous contents. Based on the spectral absorption characters of such
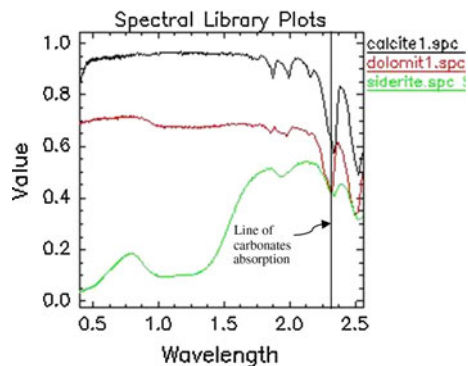
minerals, the mineral bearing rock types are discriminated over satellite data using several image processing methods including false color composites, band ratios, decorrelation stretching, and principal components analysis (Rajendran et al. 2011; Corrie et al. 2010; Ninomiya et al. 2005; Ninomiya 2002; Sultan et al. 1987).

Satellite data and methods

ASTER sensor is a multispectral imaging system, launched during December 1999 travels in a near circular, sun-synchronous orbit with an inclination of approximately 98.2°, an altitude of 705 km and a repeat cycle of 16 days. It measures visible reflected radiation in three spectral bands (VNIR between 0.52 and 0.86 μm, with 15-m spatial resolution) and infrared reflected radiation in six spectral bands (SWIR between 1.6 and 2.43 μm, with 30-m spatial resolution). It records the data in band 3B (0.76–0.86 μm) with a backward looking angle that enables the calculation of digital elevation models (DEM). In addition, it measures emitted radiation in five spectral bands in the thermal infrared region between 8.125 and 11.65 μm, with 90-m spatial resolution (Fujisada 1995). The increase of spectral bands in the SWIR region (one spectral band for Landsat
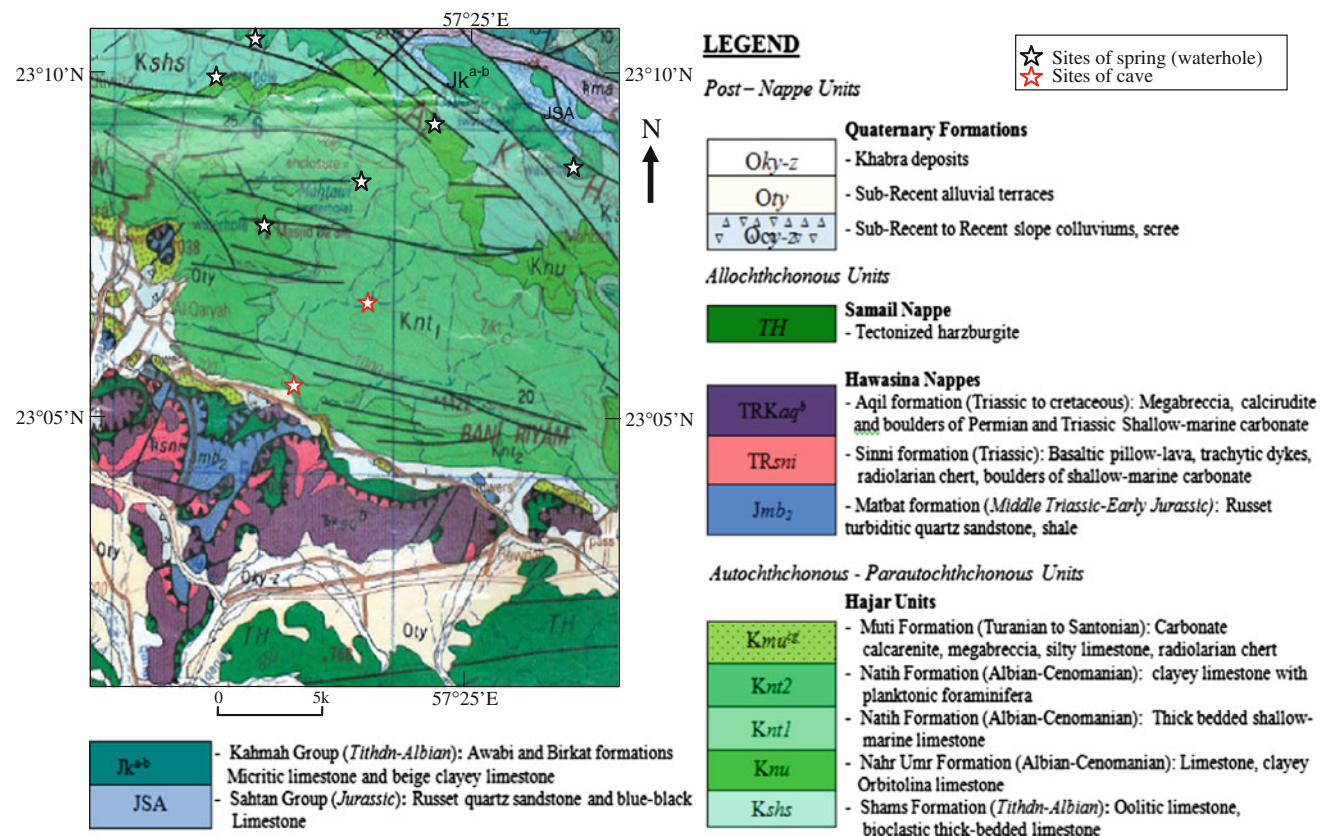

Fig. 2 USGS spectral library plots for minerals show the absorptions differences in the spectra of major carbonate minerals

Fig. 3 Geology of Site. 1 (Ministry of Petroleum and Minerals 1992)

versus six spectral bands for ASTER) enhances the surface mineralogical and lithological mapping. In the present study, 14 ASTER Level 1B spectral bands date of April 07, 2007 for Site 1 (Fig. 1b) and April 07, 2004 for Site 2 (Fig. 1c) obtained from NASA Land Processes Distributed Active Archive Center User Services, USGS Earth Resources Observation and Science (EROS) Center (https://LPDAAC.usgs.gov) are used. The data were delivered in a Tag Image File Format which provides files for each band containing the imagery and an ASCII text .met file containing the metadata. The imagery was checked and found in the cloud cover of 0 % and for sensor errors, such as banding and other geometric distortions. Both the data were supplied in terms of scaled radiance at-sensor data with radiometric and geometric corrections applied. Data were georeferenced in the UTM projection and for the WGS-84 ellipsoid. The nine VNIR–SWIR spectral bands were chosen and processed to the region of interest to map the limestone formations using ENVI (4.8) and ArcGIS (10) softwares. Mapping of limestone

formations of the study sites is carried out by decorrelation stretch digital image processing technique. Interpreted images of Site 1 and Site 2 are verified in the field, and traverse-based samples were collected for laboratory studies during May and September, 2012. The regional geological maps (Ministry of Petroleum and Minerals 1992) available in the scale 1: 250,000 were used to verify the processed remote sensing data. The samples collected from the field are studied further using a microscope and PIMA SP infrared spectrometer at the Department of Earth Sciences, Sultan Qaboos University to determine the major minerals and spectral properties of limestone formations. The spectrometer is fabricated for field spectroscopy by Integrated Spectronics Pty Ltd., Australia. It identifies and analyzes the spectral signals of rocks and minerals in the wavelength ranges from 1,300 to 2,500 nm with PIMA VIEW software (version 3.1). The spectral resolution of the instrument is ~ 7 nm. It has a built-in wavelength calibration target plate and is capable to measure spectra from 10 s to around 5-min speed.
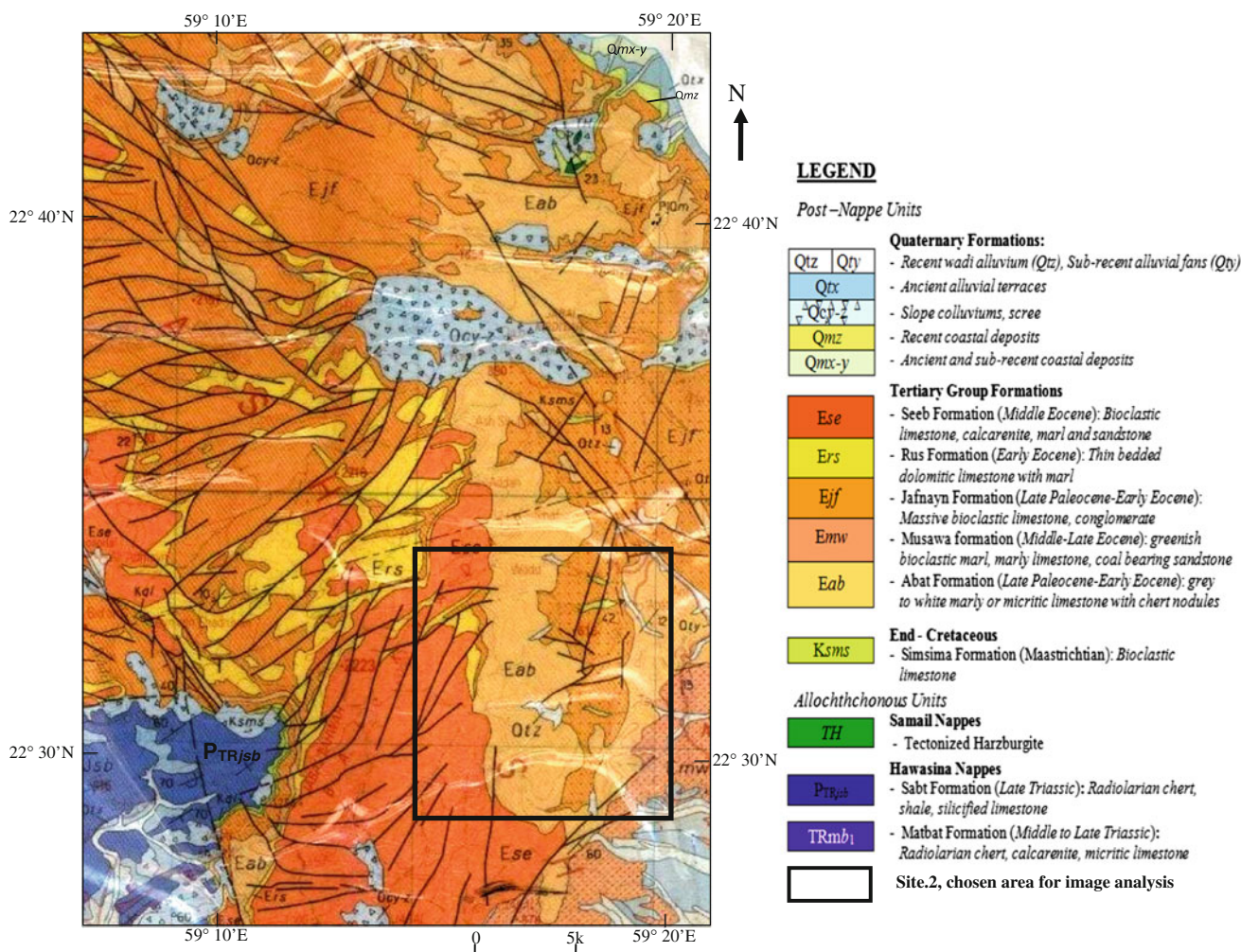

Fig. 4 Regional geology in and around of Site. 2 (Ministry of Petroleum and Minerals 1992)
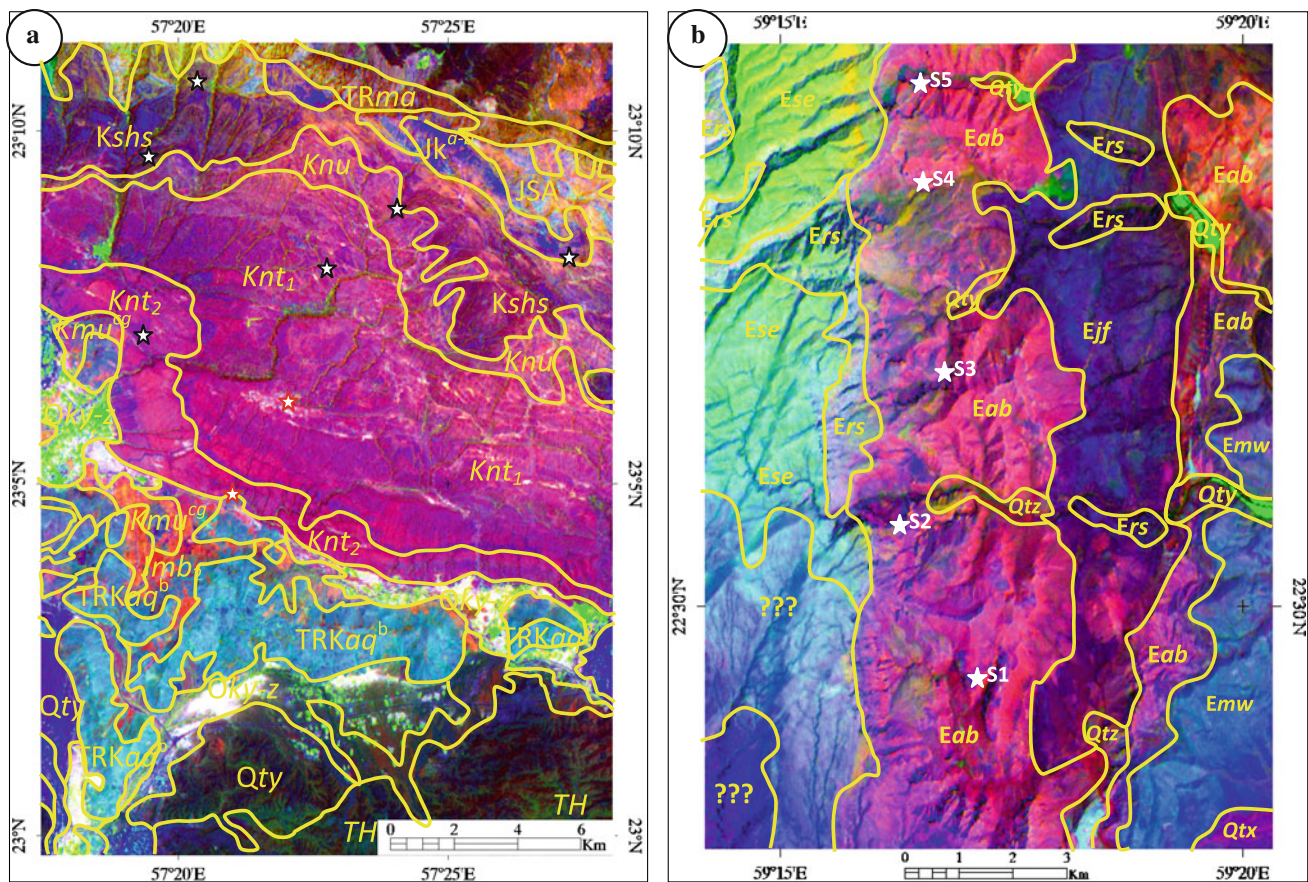
Fig. 5 Decorrelated RGB images of ASTER spectral bands 8, 3, 1 of **a** Site 1 and **b** Site 2 shows the limestone formations in pink color (refer the legend of Figs. 3, 4)

Geomorphological and geological setting

The major geomorphological units of the Site 1 (Figs. 3, 1b) are represented by structural hill (side of Jabal Akhdar anticline, Fig. 1a) and intramontane valley. The carbonate massifs are widespread over the hill area of the side of Tanuf Valley having slope environments. Occurrences of caves, springs (marked as waterhole) and dissected drainages are evidenced in this carbonate massifs (Waltham et al. 1985; Ministry of Petroleum and Minerals 1992; Hanna and Al-Belushi 1996). In Site 2 (Figs. 4 and 1b), the landscape is typically characterized by summit plateau bounded by steep structural hill slopes, which grade to wide piedmonts areas. Here, the large depressions occurred as collapsed structures. Geologically, the Site 1 consists of the major rock formations of Hajar units (Autochthonous shelf sediments), Hawasina, and Samail nappes (Allochthonous units; Fig. 3). The Sahtan and Kahmah group formations of Jurassic to Albian age of Hajar Units occurred in the NE of the area. The Shams Formation, Nahr Umr Formation, Natih Formations, and Muti Formation of

Albian to Santonian age of Hajar units cover most of the central part of the area. All formations of the Hajar Units are limestone-rich carbonate massif formations. The Hajar units are thrust over by the formations of Hawasina nappe and Samail nappe and deposited by post-nappe Quaternary formations.

The occurrences and spatial distributions of different rock formations in and around of Site 2 are given in Fig. 4. The Site 2 mainly consists of the sedimentary formations of Tertiary and Quaternary age underlined by the Allochthonous units such as Hawasina and Samail nappes (Fig. 4). Here, Simsima Formation (end of Cretaceous) is overlined by the Abat Formation, Musawa Formation, Jafnayn Formation, Rus Formation, and Seeb Formation of late Paleocene–early Eocene age. All formations are rich in limestone variety of rocks. The entire Tertiary formations are enveloped by Quaternary formations that consist of coastal deposits to recent wadi alluvium. Here, the large, oval- and crescent-shaped depressions occurred as collapsed structures in the Tertiary Group of formations (Ministry of Petroleum and Minerals 1992).

Table 1 Geographical locations of springs and caves

Locations of spring	Latitude	Longitude
WH1	23°7′6.94″N	57°27′5.67″E
WH2	23°8′33.94″N	57°28′6.86″E
WH3	23°9′13.02″N	57°24′21.13″E
WH4	23°8′57.22″N	57°24′15.50″E
WH5	23°8′46.63″N	57°23′58.60″E
WH6	23°9′13.69″N	57°23′29.99″E
WH7	23°8′28.08″N	57°23′28.64″E
WH8	23°7′49.28″N	57°24′33.91″E
WH9	23°7′32.65″N	57°23′44.94″E
WH10	23°6′43.37″N	57°24′3.33″E
WH11	23°6′31.02″N	57°24′15.75″E
WH12	23°5′54.72″N	57°23′57.53″E
WH13	23°6′17.26″N	57°22′38.32″E
WH14	23°6′16.44″N	57°22′23.16″E
WH15	23°6′22.39″N	57°22′2.59″E
WH16	23°9′23.96″N	57°20′12.15″E
WH17	23°9′28.60″N	57°20′11.85″E
WH18	23°8′46.01″N	57°18′38.77″E
WH19	23°10′4.87″N	57°18′46.23″E
WH20	23°9′33.26″N	57°17′56.09″E
WH21	23°9′32.34″N	57°17′53.15″E
WH22	23°8′39.86″N	57°17′45.59″E
WH23	23°8′39.59″N	57°17′49.37″E
WH24	23°9′40.67″N	57°15′59.33″E
WH25	23°10′8.75″N	57°15′17.58″E
WH26	23°9′55.12″N	57°15′2.09″E
WH27	23°10′6.06″N	57°14′51.94″E
WH28	23°10′10.44″N	57°14′3.42″E
WH29	23° 9′37.46″N	57°23′42.90″E
WH30	23°9′58.57″N	57°15′43.58″E
WH31	23°10′21.23″N	57°16′7.15″E
WH32	23°9′42.93″N	57°17′5.11″E
WH33	23°9′51.68″N	57°17′12.30″E
WH34	23°9′45.35″N	57°17′36.72″E
WH35	23°10′2.28″N	57°19′30.34″E
WH35	23°10′2.28″N	57°19′30.34″E
WH36	23°9′39.00″N	57°20′20.72″E
Caves		
Al Hota cave	23°6′6.03″N	57°22′6.20″E
Al Fallah Cave	23°4′55.60″N	57°21′15.98″E

Mapping of limestone formations

The occurrences and spatial distribution of limestone formations are mapped by decorrelation stretch digital image processing method, studying the spectral sensitivities of carbonate minerals (as discussed above in Sect. 2) of the formations using ASTER spectral bands 8 (2.295–2.365 µm), 3 (0.78–0.86 µm), and 1(0.52–0.60 µm) for Site 1 and Site 2. Among the three bands, the band 8 responds to the presence of carbonate and hydroxyl bearing minerals of the limestone formations. Band 3 serves to characterize the general albedo of the materials to highlight certain silicate minerals associated with the formations and band 1 contains information relating to the presence of iron minerals associated with the formations or tectonized harzburgite. The technique is well discussed by Gillespie et al. (1986), Rothery (1987a, b) and Abrams et al. (1988), which is based on principal components transformation of the acquired data. The transformed channels here are themselves contrasted, stretched, and arbitrarily assigned to primary colors for display as a color composite image.

The images of decorrelated ASTER bands 8, 3, and 1 of the study sites are given in Fig. 5. Almost all limestone formations occurred in Tanuf Valley (Figs. 1b, 3, 5a) and Sur region (Figs. 1c, 4, 5b) of the parts of Oman are discriminated well. The formations are mapped and are correlatable to the available geological maps (Figs. 3, 4). The limestone formations of Tanuf Valley namely Shams (Kshs), Nahr (Knu), Natih (K$nt1$ and K$nt2$), and Muti (Kmu^{cg}) Formations of Albian to Santonian age are well delineated within Hajar units. The occurrence and spatial distribution of formations are shown distinctly by pink color in the decorrelated RGB image (Fig. 5a). The other formations associated with massifs, such as Hawasina and Samail post-nappe units, are discriminated by pale blue and dark green colors, respectively. The limestone formations have the occurrences of springs and caves (Figs. 3, 5a) and their locations are star marked on the interpreted image (Fig. 5a). These features were studied and discussed in the field in the following section. The Natih formations are major oil producing formations in Oman and featured by the occurrences of Al Hota and Al Fallah caves (Hanna and Al-Belushi 1996; Frans et al. 2002). The decorrelated RGB image of Site 2 of Sur region (Fig. 5b), which consists of the Tertiary group formations, namely Abat (Eab), Musawa (Emw), Jafnayn (Ejf), Rus (Ers), and Seeb (Ese), are discriminated too well similar to Site 1. The occurrence and spatial distribution of such carbonate formations are shown by similar pink color. Interpretations of image show the occurrences of large depressions at the boundary between the Abat and Seeb Formations (Figs. 3, 5b). The locations of such depressions are star marked on the interpreted image (Fig. 5b). The image processing method applied on ASTER spectral bands (8, 3, and 1) are proved beneficial in the discrimination of limestone formations of the study sites.
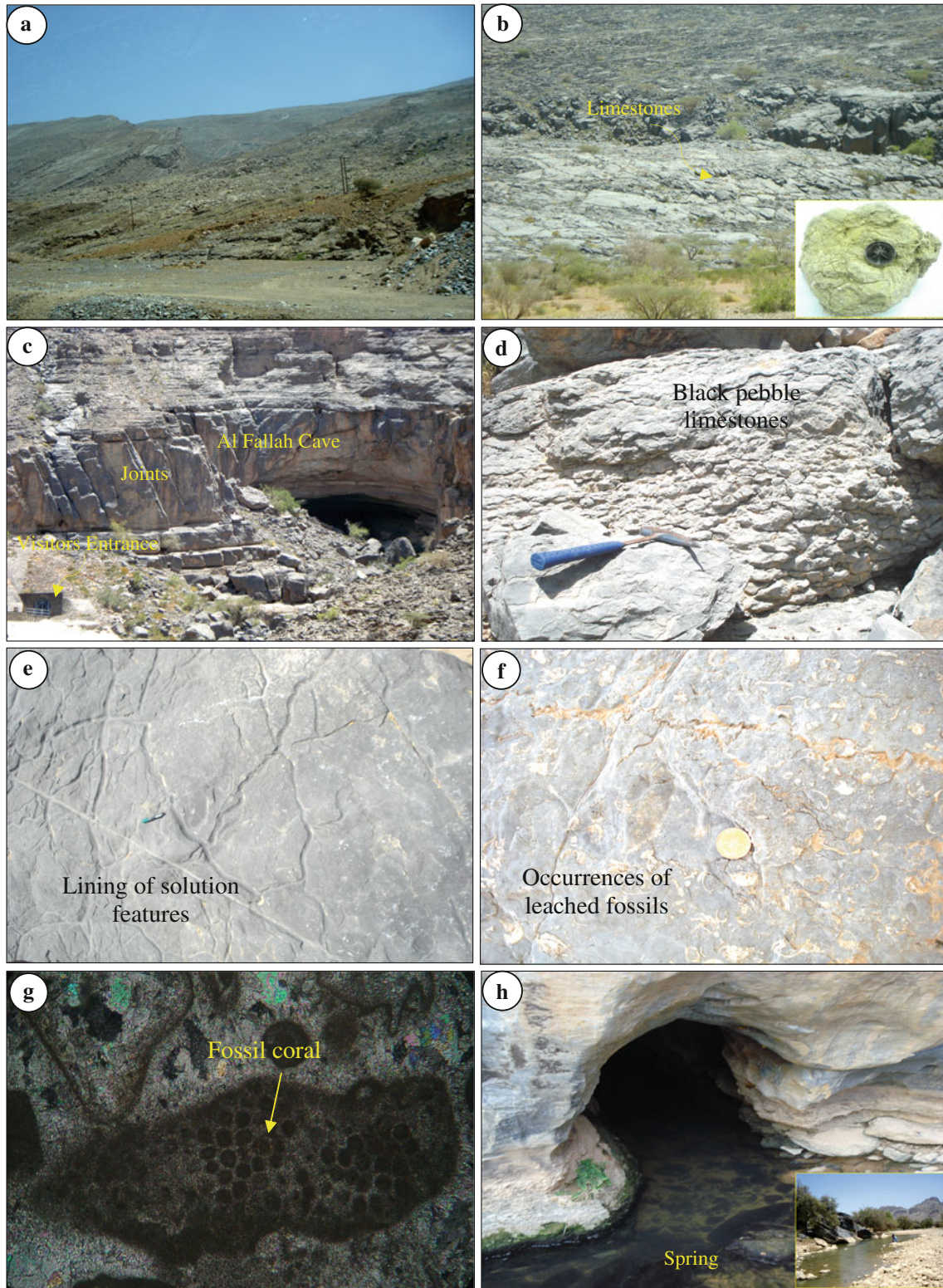
Fig. 6 Field photographs in and around of Tanuf Vally shows **a** the steep dipping of the Natih formations, **b** the massive and smooth surface Natih formations, **c** the Al Fallah cave in Natih formations, **d** the black pebble in limestone, **e** the lining of solution features in dolomites, **f** the occurrences of fossils on the surface of dolomites, **g** the dissolved coral filled with sediment occurred in carbonate massif observed under the microscope (nicols crossed 25×), and **h** the spring in the lower part of Natih formations
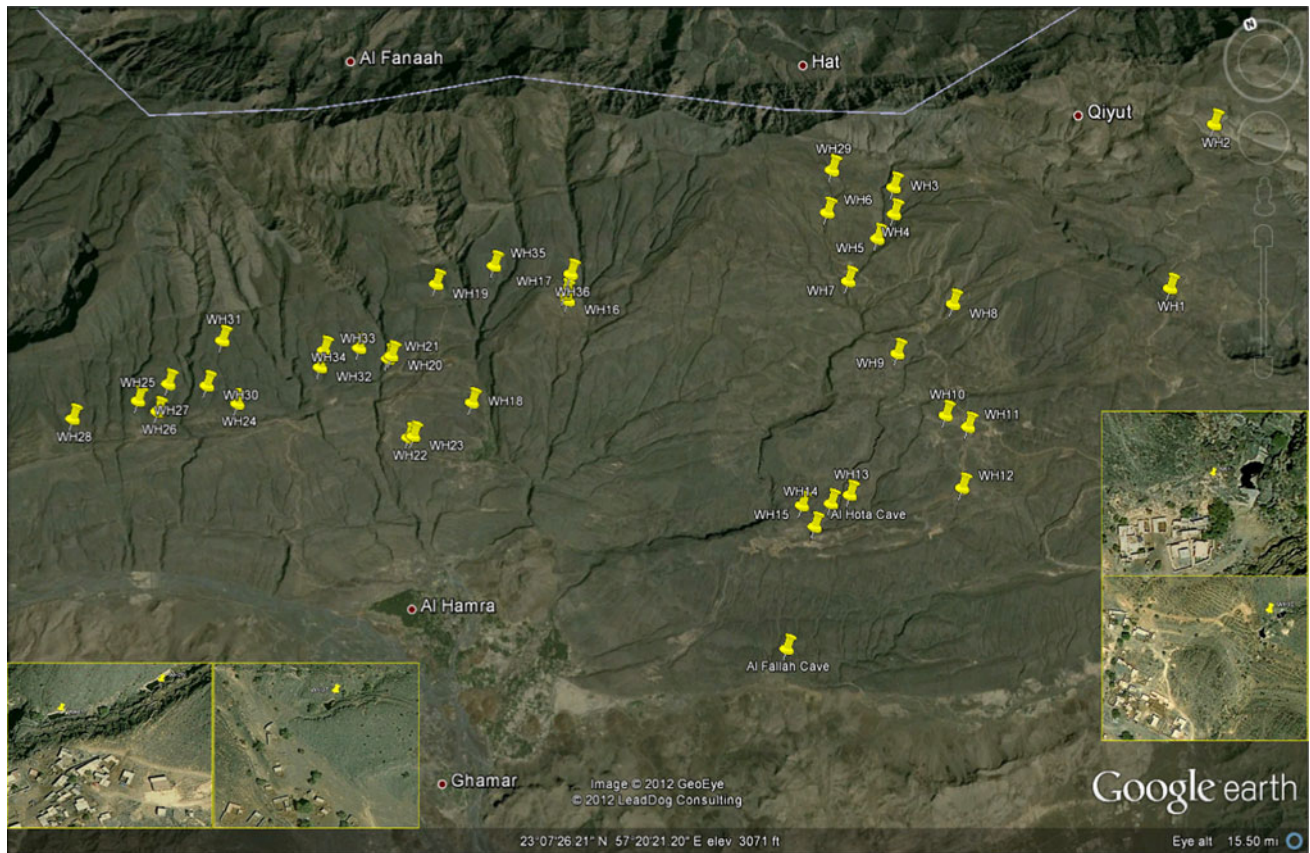
Fig. 7 Google Earth true color satellite image shows the locations of spring in the carbonate massifs at Anuf Valley (*inset* shows the springs of location WH1, WH10, WH20, WH21 and WH27)

Field evidences and laboratory studies

Systematic field verifications on interpreted image of Site 1 and Site 2 are carried out and traverse-based samples were collected. The occurrences of carbonate massifs and associated rock types of Tanuf Valley and Sur region discriminated on the image by difference in tones are verified at several locations. The samples used in the laboratory studies are described in Table 1. At Tanuf Valley, the Natih formations (K*nt1*, K*nt2*) of Hajar units are shelf carbonate sedimentary rocks deposited during Albian to Cenomanian age widespread over a large area from the base of Tanuf valley (Hanna and Al-Belushi 1996; Frans et al. 2002). In the field, these are dipping steep and developed slope to the side of Tanuf Valley (Fig. 6a). The K*nt1* formation is thick and its surface is massive and smooth (Fig. 6b) compared to K*nt2* formation, which may be due to the presence of high contents of dolomite formed by dolomitization. The formations consist of gray to black limestone and dolomites (Table 1; Vandeginste and John 2012; Breescha et al. 2006; Frans et al. 2002; Pratt and Smewing 1990; Filbrant et al. 1990). These are massive and karstified due to the circulation of water (Hillgärtner

Table 2 Geographical locations of depressions

Locations of depression	Latitude	Longitude
S1	22°29′23.33″N	59°16′50.71″E
S2	22°30′52.65″N	59°16′6.46″E
S3	22°31′39.61″N	59°16′19.82″E
S4	22°33′12.31″N	59°16′2.50″E
S5	22°34′10.83″N	59°16′25.28″E
S6	22°34′45.34″N	59°16′28.52″E
S7	22°36′0.50″N	59°16′0.11″E
S8	22°37′10.11″N	59°15′18.90″E
S9	22°38′40.95″N	59°14′52.51″E
S10	22°40′34.74″N	59°18′15.58″E
S11	22°43′5.77″N	59°18′5.37″E
S12	22°45′47.55″N	59°15′38.08″E
S13	22°47′45.00″N	59°13′55.58″E
S14	22°43′30.38″N	59°8′51.43″E
S15	22°54′0.31″N	59°5′27.53″E
Bimmah waterhole	23°2′7.72″N	59°4′21.59″E

et al. 2003; Sattler et al. 2005). The occurrences of Al Hota and Al Fallah caves are occurred within these formations (Fig. 6c; Hanna and Al-Belushi 1996). They are the
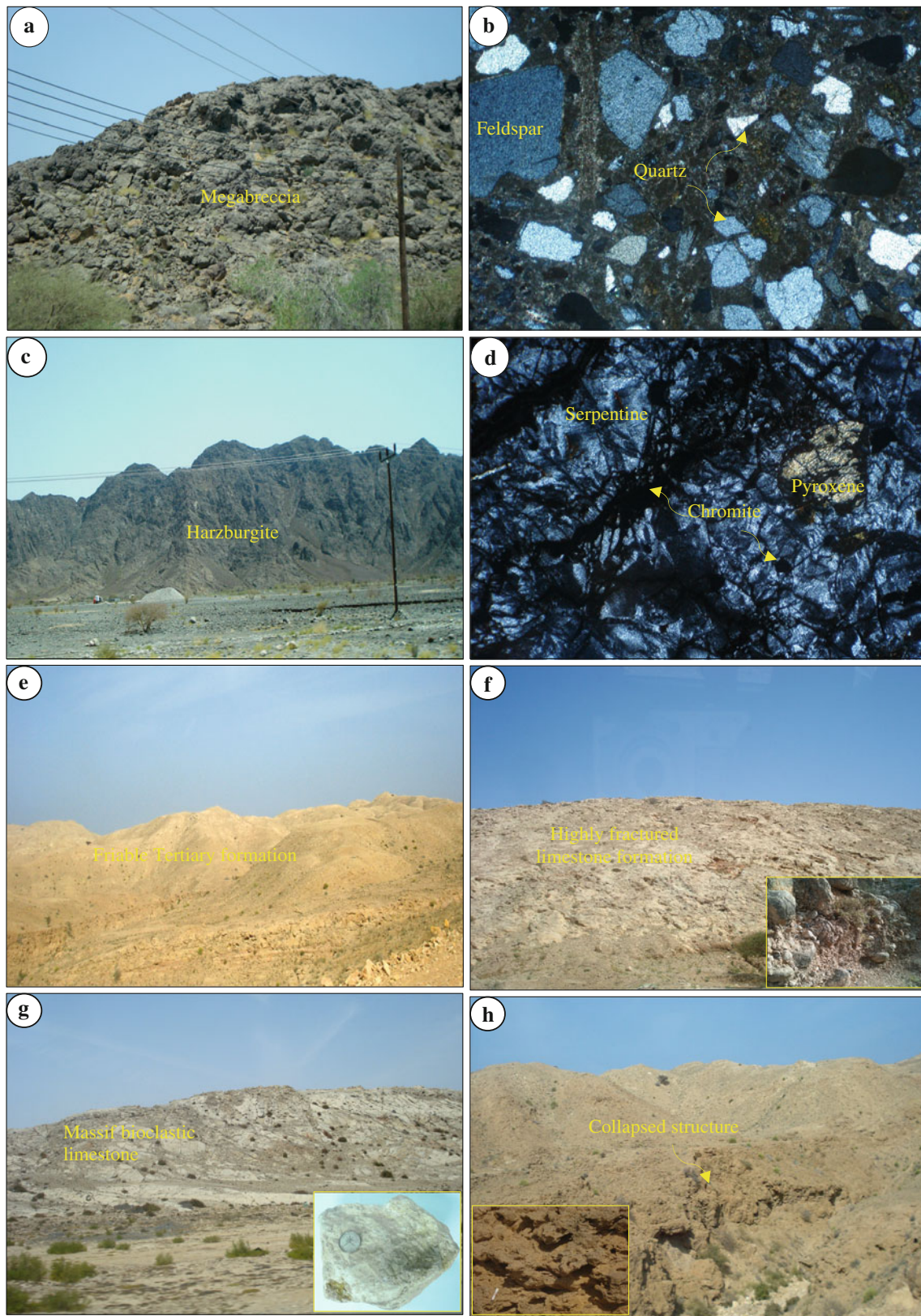
Fig. 8 Filed photographs shows the occurrences of **a** the megab-reccia of Aqil formation in filed and **b** under microscope (nicols crossed, 15×), **c** the tectonized harzburgite of Samail nappe in field and **d** under microscope (nicols crossed, 25×) of Tanuf Valley, and **e** friable Tertiary formations, **f** and **g** limestone massifs, and **h** the collapsed structure of Sur region
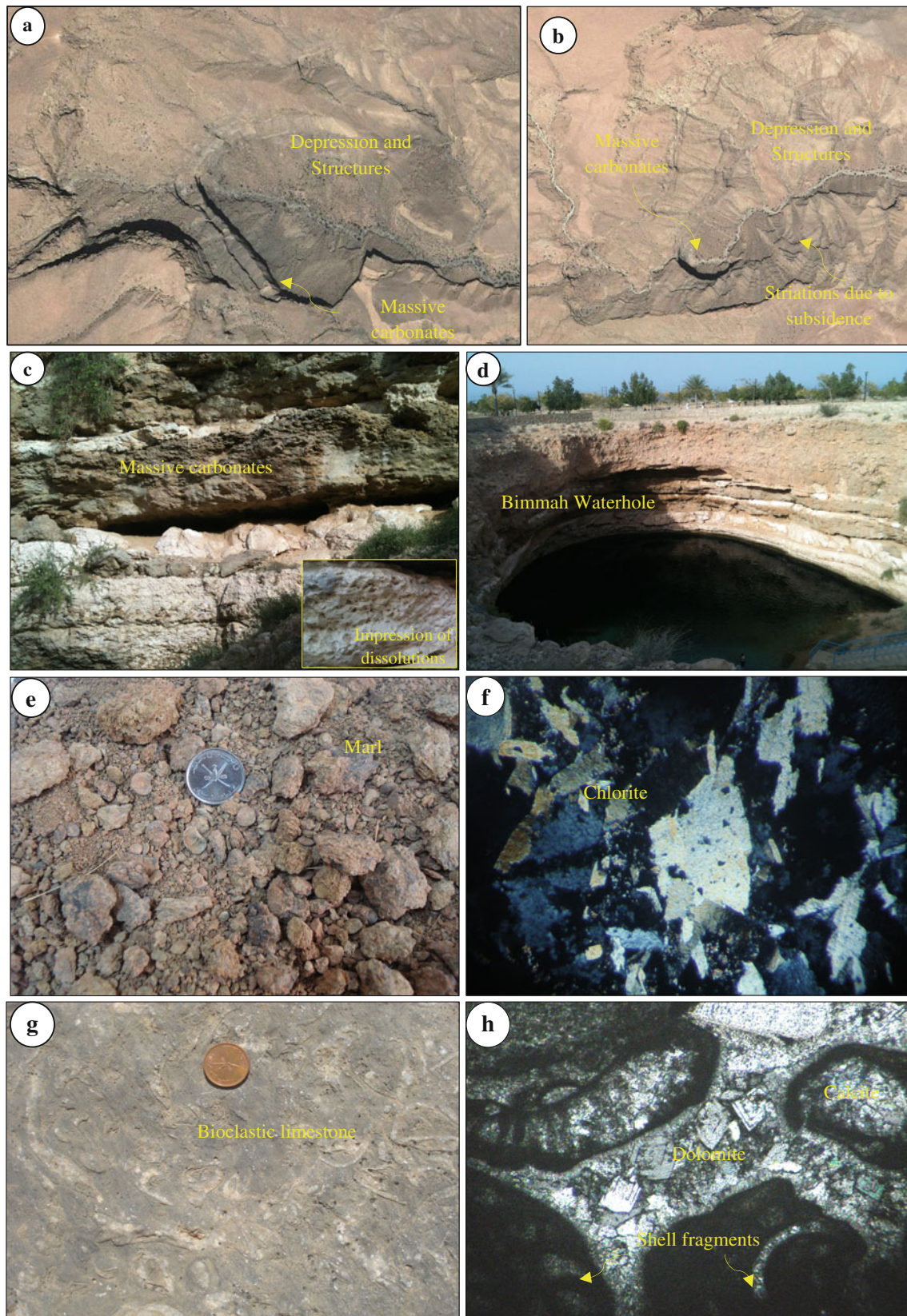
Fig. 9 Shows **a** and **b** the depressions (S1 and S5 in Fig. 5b) and massive carbonates over the Google image (not to scale), **c** the photographs of massive carbonates with dissolution imprints, **d** the deep waterhole (Bimmah), **e** the marl in the field and **f** the marl under the microscope (nicols crossed 25×), **g** the massive bioclastic limestone in the field and **f** under the microscope (nicols crossed 25×) of Sur region

occurrence of speleothems in caves (http://www.alhota caves.com) and solutional karst features in the limestone surface, such as black pebble limestones (Fig. 6d), lining of solution features (Fig. 6e), extensive dissolution, missing fossilized zones, and leached fossils surface (Fig. 6f; Jones and Smith 1987; Wright 1982) are observed in the field. Under the microscope, the dissolved corals filled with sediments (Fig. 6g) are observed. The occurrences of springs are evidenced (Fig. 6h) in parts of Natih formations (K*nt1*). The survey made with the local people, confirms that these are being used for domestic and irrigational purposes. Visual interpretations of true color Google Earth images (http://www.google.com/earth/index.html) of the region show the occurrences of more springs (WH1–WH36) in the barren exposures of massif formations and are located in Fig. 7. The geographical locations of the caves and springs of the region are given in Table 2. Detailed study and investigation of these features in the entire formations of Hajar units of this region using high spatial resolution satellite data may provide significant useful information to the socio-economic and cultural development of this region. The other rock types, such as megabreccia (TRK*aq*^{b}) of Aqil formation of Hawasina nappe and tectonized harzburgite (*TH*) of Samail nappe

(post-nappe units) associated with Natih formations, are verified in the field and the samples are studied under the microscope. The field structure of megabreccia (Fig. 8a) exhibits coarse mosaic texture and pale blue in color on the image (Fig. 5a) which is easily distinguishable from its associated rocks. Under the microscope, the minerals of the rock show angularities (Fig. 8b). The harzburgite is interpreted from dark green in color (Figs. 5a) on the image and tectonized in the field (Fig. 8c). Under the microscope, the major minerals, such as serpentine and orthopyroxene (Fig. 8d), are studied. Chromite is observed as minor phases.

In the field, the limestone formations of Site 2 are friable (Fig. 8e), fractured and massifs, occurred in different thicknesses (Fig. 8f). The image interpretations of Abat Formations that consists of gray to white marly or micritic limestone with chert nodules and overlined by the Seeb Formations, consists of bioclastic limestone (Fig. 8g), calcarenite, marl, and sandstone are verified in the field. The occurrences of large depressions as collapsed structures (Fig. 8h) at the boundary between Abat and Seeb formations are observed (Fig. 9a, b). The region exhibits a wider plateau at the top and a steep slope at the boundary. The collapsed breccias and extensive dissolution on the
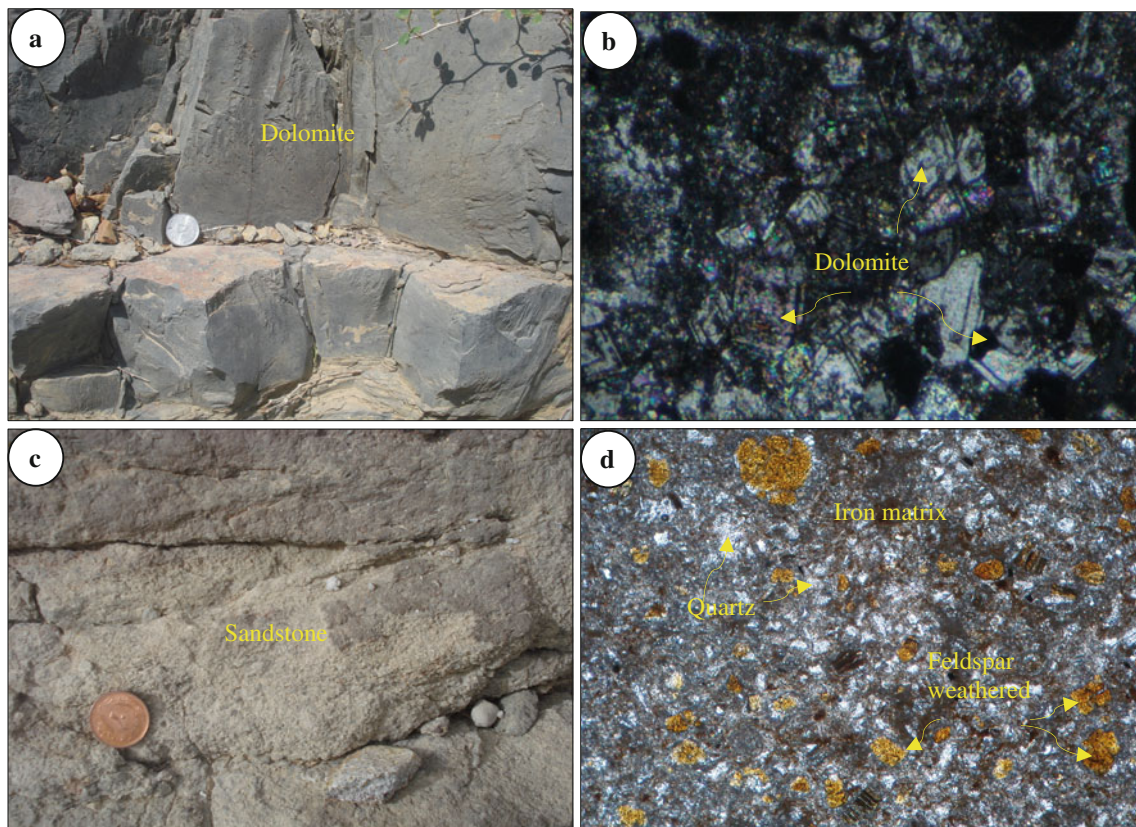

Fig. 10 Photographs of Sur region shows the occurrences of **a** dolomite in the field and **b** under the microscope (nicols crossed 25×), **c** sandstone in the field, and **d** under the microscope (nicols crossed 25×)

Table 3 Shows the locations and descriptions of selected samples collected from the field

No.	Locations		Field descriptions		Laboratory minerals descriptions	
	Latitude	Longitude	Types	Characters	Microscopic	Spectrometer
At Tanuf Valley						
AH1	23°04′47″N	57°21′16″E	Dolomite	Massive	Rich in dolomite, calcite	Dolomite
AH2	23°04′47″N	57°21′14″E	Clayey Limestone	Clay, friable	Clay minerals	Montmorillonite, calcite
AH3	23°05′22″N	57°19′53″E	Dolomite	Massive	Rich in dolomite, calcite	Dolomite
AH5	23°06′13″N	57°22′10″E	Limestone	Friable	Rich in calcite, dolomite	Limestone
AH5a	23°06′17″N	57°22′04″E	Limestone	Massive	Rich in calcite, dolomite	Limestone
At Sur Region						
Sr3	22°30′53″N	59°17′02″E	Limestone	Massive,	Rich in dolomite, calcite	Dolomite
Sr5	22°28′47″N	59°16′52″E	Marl limestone	Massive, friable	Cemented, calcite, clay minerals	Montmorillonite, dolomite
Sr6	22°29′04″N	59°16′43″E	Marl limestone	Friable	Calcite, clay minerals	Montmorillonite, calcite
Sr9	22°28′32″N	59°18′32″E	Marl sandstone	Loose and friable, ferrugenous	Sharp, iron-stained border, zone of micrite, chlorite	Montmorillonite, siderite
Sr10	22°30′50″N	59°16′25″E	Limestone	Massive	Calcite, dolomite coral	Dolomite
Sr12	22°30′44″N	59°19′12″E	Limestone	Massive	Rich in dolomite, calcite	Dolomite
Sr15	22°38′36″N	59°20′26″E	Marl Limestone	Massive, friable, bioclasts	Calcite rich fossiliferous	Calcite
Sr16	22°39′09″N	59°20′50″E	Marl Limestone	Loose and friable	Calcite, clay minerals	Calcite, montmorillonite, tremolite

carbonate massifs are observed in the field. The depressions are developed due to the movement of Seeb formations into voids created by the dissolution of water in the limestones of Abat formations. Here, the bioclastic limestones occurred as massive formations (Fig. 9c). The region is also featured by a deep water hole (Bimmah) developed by the collapse of limestone cavern (Fig. 9d). The samples of marl (Fig. 9e), massive bioclastic limestone (Fig. 9 g), dolomite (Fig. 10a), and sandstone (Fig. 10c) collected from the field are studied in the laboratory. The microscopic study of such samples shows the presence of more chlorite minerals in the marl (Fig. 9e, f), bioclasts in the bioclastic limestone (Fig. 9 g, h), minerals of dolomite (Fig. 10a, b), and sandstone (Fig. 10c, d). Under the microscope, the etched carbonate cements are studied. The grain boundaries are marked by sharp, iron-stained border, a zone of micrite that contains some iron staining (Jones and Smith 1987; Wright 1982). Study of the true color Google Earth image shows the occurrences of 15 large depressions along the boundary in and around this region. The geographical locations of the depressions are given in Table 3.

Further, the samples collected from the field are studied for the understanding of the image characters of limestone formations by measuring the spectral reflectances using PIMA SP infrared spectrometer. The spectral plots of selected samples of Tanuf Valley (Sample nos. AH1, AH2, AH3, AH5, and AH5a) and Sur region (Sample nos. Sr3,

Sr5, Sr6, Sr9, Sr10, Sr12, Sr15, and Sr16) are given in Fig. 11. Almost all the samples showed strong absorptions around 2.3 μm and confirmed the presence of carbonate minerals namely calcite ($CaCO_3$; Fig. 11a), dolomite [$CaMg(CO_3)_2$; Fig. 11b], and siderite ($FeCO_3$; Sample no. Sr. 9, marl sandstone). The montmorillonites [$(NaCa)_{0.33}$ $(AlMg)_2$ $(Si_4O_{10})(OH)_2 . nH_2O$] are detected with carbonate minerals in the marl samples. It shows a strong absorptions feature around 1.4 and 1.9 μm in the infrared wavelength regions (Fig. 11c) due to the presence of hydroxyl molecules in its contents. The selected plots of calcite, dolomite, and montmorillonite minerals are given in Fig. 12 to compare the absorption differences of minerals. It shows that the samples containing high content of calcite have strong absorptions compared to the samples consisting of dolomite and montmorillonite which have moderate to poor absorptions. The absorptions of dolomite and montmorillonite are due to the presence of magnesium and hydroxyl molecules in its contents, respectively.

Conclusions

In the present study, the limestone karst formations of Tanuf Valley and Sur regions are discriminated well by the decorrelated image processing methods using ASTER spectral bands 8, 3, and 1. The discriminations are carried out based on the spectral sensitivity of carbonate minerals which have
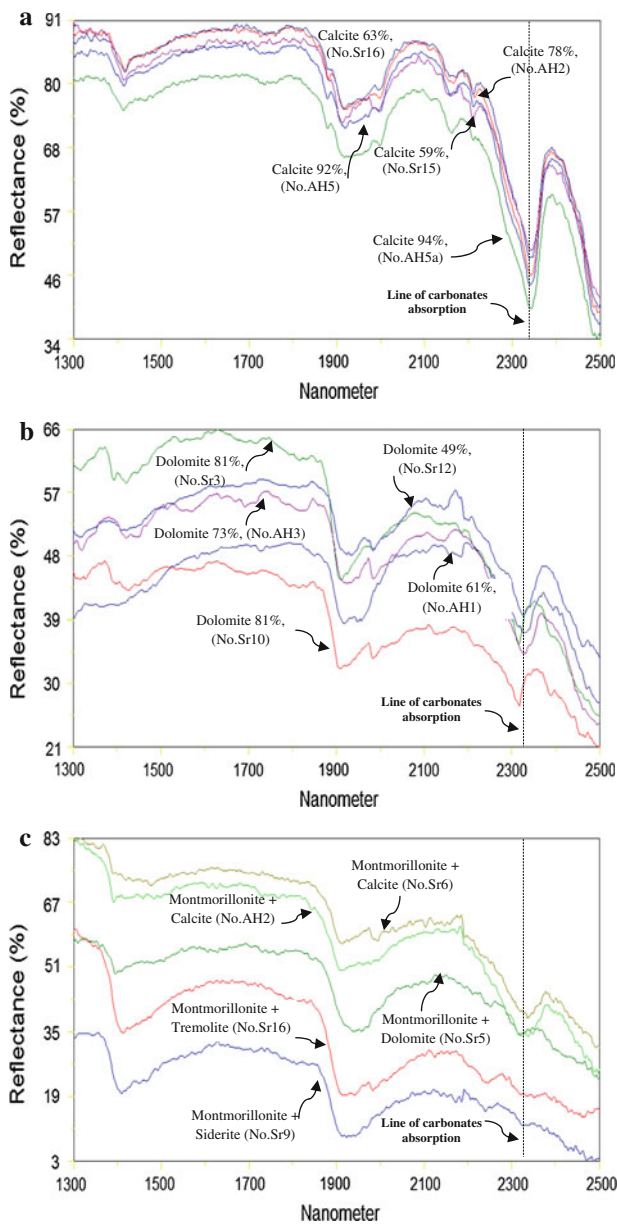
Fig. 11 Spectral plots show the absorption features of **a** calcite, **b** dolomite, and **c** montmorillonite minerals in the carbonate massifs of study sites

Fig. 12 Spectral plots compare the absorptions of carbonate minerals

Earth image. The samples collected from the field are studied in the laboratory and the mineralogical and spectral characters of carbonate formations are confirmed. Thus, the study of mapping of limestone formations of the study sites using ASTER spectral bands by decorrelated stretch image processing method demonstrates the capability of ASTER sensor; and thus, the technique presented in this work could be applied to other geographical regions where similar questions needed to be resolved.

CO_3 absorption near 2.35 μm in ASTER band 8. The interpretations of limestone formations and associated lithologies of sites are comparable with the available geological map. The limestone formations of Albian–Cenomanian periods of Cretaceous age of Tanuf Valley are associated with the Hawasina and Samail nappes whereas, the limestone formations of Tertiary age (late Paleocene to early Eocene) of Sur region are associated with Hawasina and Samail nappes and Quaternary formations. Caves, springs and large depressions that occurred in limestone formations in the sites are studied in the field and the more occurrences of springs and depressions are interpreted and located on the Google
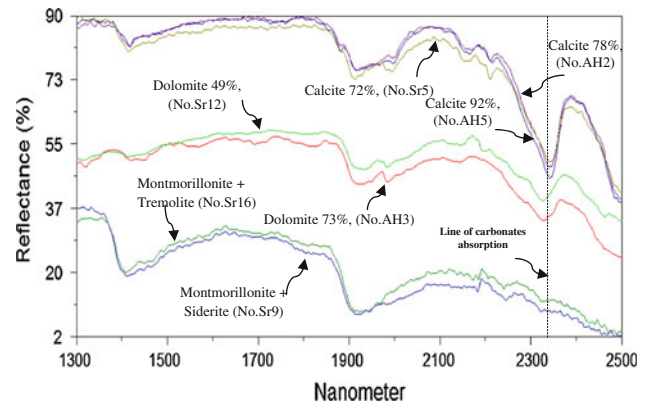
References

Abdeen MM, Allison TK, Abdelsalam MG, Stern RJ (2001) Application of ASTER band-ratio images for geological mapping in arid regions; the Neoproterozoic Allaqi Suture, Egypt. Abstract with Program Geological Society of America 3(3):289

Abrams MJ, Rothery DA, Pontual A (1988) Mapping in the Oman Ophiolite using enhanced Landsat Thematic Mapper images. Tectonophysics 151:387–401

Beck BF (1984) Sinkholes terminology. In: Beck BF (ed) Sinkholes, their geology, engineering and environmental impact. Balkema, Rotterdam, p 429

Breescha L et al (2006) Dolomite formation in breccias at the Musandam Platform border, Northern Oman Mountains, United Arab Emirates. J Geochem Explor 89(1–3):19–22

Clark RN (1999) Spectroscopy of rocks and minerals, and principles of spectroscopy. In: Rencz A (ed) Manual of remote sensing, vol 3. Wiley, New York, pp 3–58

Combe JP, Launeau P, Pinet P, Despan D, Harris E, Ceuleneer G, Sotin C (2006) Mapping of an ophiolite complex by high-

resolution visible–infrared spectrometry. Geochem Geophys Geosyst 7(8):1–11

Corrie RK, Ninomiya Y, Aitchison JC (2010) Applying advanced spaceborne thermal emission and reflection radiometer (ASTER) spectral indices for geological mapping and mineral identification on the Tibetan Plateau. Int Arch Photogramm Remote Sens Spat Info Sci XXXVIII(8):464–469

Filbrant JB, Nolan SC, Ries CA (1990) Late Cretaceous and early Tertiary evolution of Jebel Ja'alan and adjacent areas, NE Oman. The Geology and Tectonics of the Oman Region. Geol Soc Spec Pub 49:697–714

Frans SP, Van Buchem, Philippe R, Peter WH, Oterdoom W Heiko, Philip Jean (2002) Stratigraphic organization of carbonate ramps and organic rich intra-shelf basins: natih Formation (middle Cretaceous) of northern Oman. AAPG Bulletin 86(1):21–53

Fujisada H (1995) Design and performance of ASTER instrument. Proc SPIE Int Soc Opt Eng 2583:16–25

Gillespie AR, Kahle AB, Walker RE (1986) Color enhancement of highly correlated images. 1. Decorrelation and HSI contrast stretches. Remote Sens Environ 20:209–735

Gomez C, Delacourt C, Allemand P, Ledru P, Wackerle R (2005) Using ASTER remote sensing data set for geological mapping, in Namibia. Phys Chem Earth 30:97–108

Hanna S, Al-Belushi M (1996) Introduction to caves of Oman. Sultan Qaboos University, Oman, pp 49–62

Hillgärtner H, Buchem FSP, Gaumet F, Razin P, Pittet B, Grotsch J, Droste H (2003) The Barremian–Aptian evolution of the Eastern Arabian carbonate platform margin (Northern Oman). J Sediment Res 73(5):756–773

Hunt GR (1977) Spectral signatures of particulate minerals in the visible and near infrared. Geophysics 42(3):501–513

Jalali N, Saghafian B, Imanov F, Museyyibov M (2009) Recognition of shallow karst water resources and cave potentials using thermal infrared image and terrain characteristics in semi-arid regions of Iran. Int J Appl Earth Obs Geoinformation 11:439–447

Jones B, Smith DS (1987) Open and filled karst features on the Cayman Islands: implications for the recognition of paleokarst. Can J Earth Sci 25:1277–1291

Kuosmanen V, Laitinen J, Arkimaa H, Kuosmanen E (2000) Hyperspectral characterization of selected remote detection targets in the mines of HYDO partners. Geological Survey of Finland, Archive report RS/2000/02

Mars JC, Rowan LC (2010) Spectral assessment of new ASTER SWIR surface reflectance data products for spectroscopic mapping of rocks and minerals. Remote Sens Environ 114:2011–2025

Ministry of Petroleum and Minerals (1992) Geological Map, Oman (1:250,000). SEEB Sheet NF 40-03

Ninomiya Y (2002) Mapping quartz, carbonate minerals and mafic-ultramafic rocks using remotely sensed multispectral thermal infrared ASTER data. P SPIE 4710:191–202

Ninomiya Y, Fu B, Cudahy TJ (2005) Detecting lithology with Advanced Spaceborne Thermal Emission and Reflection Radiometer (ASTER) multispectral thermal infrared "radiance-at-sensor" data. Remote Sens Environ 99:127–139

Pratt BR, Smewing JD (1990) Jurassic and Early Cretaceous platform margin configuration and evolution, central Oman Mountains. The geology and tectonics of the Oman Region. Geol Soc Spec Pub 49:69–88

Rajendran S, Hersi OS, Al-Harthy AR, Al-Wardi M, El-Ghali MA, Al-Abri AH (2011) Capability of Advanced Spaceborne Thermal Emission and Reflection Radiometer (ASTER) on discrimination of Carbonates and associated rocks and Mineral Identification of Eastern Mountain region (Saih Hatat Window) of Sultanate of Oman. Carbonates Evaporites 26:351–364

Robertson AHF, Searle MP (1990) The northern Oman Tethyan continental margin: stratigraphy, structure, concepts and controversies The Geology and Tectonics of the Oman Region. The geological society, London, vol 49, pp 3–25

Rothery DA (1987a) Improved discrimination of rock using Landsat Thematic Mapper imagery of the Oman ophiolite. J Geol Soc London 144:587–597

Rothery DA (1987b) Decorrelation stretching an aid to image interpretation. Int J Remote Sens 8:1253–1254

Rowan LC, Mars JC (2003) Lithologic mapping in the mountain pass, California area, using advanced space borne thermal emission and reflection radiometer (ASTER) data. Remote Sens Environ 84(3):350–366

Sattler U, Immenhauser A, Hillgärtner H, Esteban M (2005) Characterization, lateral variability and lateral extent of discontinuity surfaces on a carbonate platform (Barremian to Lower Aptian, Oman). Sedimentology 52:339–361

Sauro U (2003) Dolines and sinkholes: aspects of evolution and problems of classification. Acta carsologica 32(2):41–52

Siart C, Bubenzer O, Eitel B (2009) Combining digital elevation data (SRTM/ASTER), high resolution satellite imagery (Quickbird) and GIS for geomorphological mapping: a multi-component case study on Mediterranean karst in Central Crete. Geomorphology 112:106–121

Sinclair WC, Stewart JW (1985) Sinkhole type, development, and distribution in Florida. Map Series No. 110. Florida Department of Natural Resources, Bureau of Geology, Tallahassee, Florida

Sultan M, Arvidson RE, Sturchio NC, Guinnes EA (1987) Lithologic mapping in arid regions with Landsat TM data: Meatiq dome, Egypt. Geol Soc Am Bull 99:748–762

USGS Mineral Spectral Library. http://www.speclab.cr.usgs.gov

Vandeginste V, John CM (2012) Influence of climate and dolomite composition on dedolomitization: insights from a multi-proxy study in the central Oman Mountains. J Sediment Res 82(3):177–195

Waltham AC, Brown RD, Middleton TC (1985) Karst and caves in the Jabal Akhdar, Oman. Cave Sci 12:69–79

Waltham T, Bell F, Culshaw M (2005) Sinkholes and subsidence. Karst and Cavernous Rocks in Engineering and Construction. Praxis Publishing, Chichester, p 382

Williams P (2003) Dolines. In: Gunn J (ed) Encyclopedia of caves and karst science. Fitzroy Dearborn, New York, pp 304–310

Wright VP (1982) The recognition and interpretation of paleokarsts: two examples from the Lower Carboniferous of South Wales. J Sediment Petrol 52:83–94